MODELLING HYDROGEN FUEL CELL AIRCRAFT IN SUAVE

Christian Svensson¹, Petter Miltén¹ & Tomas Grönstedt¹

¹Division of Fluid Dynamics, Department of Mechanics and Maritime Sciences, Chalmers University of Technology, Gothenburg, 412 96, Sweden

Abstract

Methods for conceptually designing and assessing the mission performance of regional hydrogen fuel cell aircraft are implemented in the open-source software SUAVE. In order to design for and assess the performance in future operations, methods for sizing representative propulsion and fuel storage systems are implemented. Additionally, algorithms for airframe resizing are added in order to account for mass and geometry changes when redesigning existing regional aircraft for fuel cell propulsion. Dynamic methods for the fuel cell power demand and tank thermodynamics are implemented in order to asses the effect of fuel consumption and hydrogen boil-off on the aircraft's mission performance. A set of tanks are designed for a fixed fuselage geometry to investigate the effect of fuel volume and number of tanks on tank gravimetric index (GI). A large fuel volume requires non-spherical tanks, which significantly lowers GI, and therefore increasing the number of tanks can be beneficial. An ATR42 regional turboprop is redesigned for fuel cell propulsion and liquid hydrogen stored in two aft-mounted tanks. A fuselage extension of 16% and reference area increase of 6% are needed for 6 m³ of fuel at maintained wingloading and power-to-weight ratio. MTOW increased by 6% and exhibits a shift in center-of-gravity of 5.5% between MTOW and MZFW conditions.

Keywords: hydrogen, aircraft resizing, proton-exchange membrane fuel cell, multi-layer insulation, SUAVE

1. Introduction

Decarbonizing global air travel will require the implementation of a large range of different energy sources and propulsion architectures [1]. It is estimated that regional aircraft have an 80% higher CO₂ intensity (kg per passenger-kilometer) than narrow and widebody aircraft, which is thought to stem from improvement efforts being prioritized for longer range aircraft [2]. Furthermore, passenger flights under 1000 NM are estimated to produce a third of global CO₂ emissions [2]. The use of hydrogen as aviation fuel will therefore be a key enabler to future CO₂ emission-free flights in the short to medium-range market.

The Cryoplane-project [3] conducted in the early 2000's was able to demonstrate high technical feasibility for their proposed hydrogen fleet, but concluded the economic factor to be of most hindrance. In a study on refueling infrastructure for small and large airports in a year 2050 scenario [4], it was estimated that the price of liquid hydrogen (LH₂) would match that of kerosene if the price of kerosene was increased by 110% at small airports and 56% at large airports. This makes short-range flights to small airports economically challenging.

In addition to the high cost of refueling at smaller airports, the availability of hydrogen refueling infrastructure might be limited in the early stages of a transition to hydrogen flight. If refueling capability is limited to major airline hubs, many short-range routes where hydrogen could make a significant impact might be eliminated. This unless the aircraft is designed for so called "return-without-refuel" operation, i.e. returning from the destination airport on the same tank of fuel.

Conventional turboprop aircraft in the 50 to 70 PAX range today serve many routes below 800 NM and could be modified for liquid hydrogen storage and fuel cell electric propulsion. This would offer a relatively low-risk option for operators and could help accelerate the transition to hydrogen. In order for this type of aircraft to operate in sparse hydrogen infrastructure, the design of the LH₂ tanks becomes an area of great significance. Hence, a comprehensive simulation environment is needed to enable balanced designs optimal for the market requirements. This paper outlines new implementations in the conceptual aircraft design tool SUAVE [5, 6]. This includes routines for designing and resizing regional hydrogen fuel cell aircraft and dynamic propulsion models integrated in the mission solver.

2. Hydrogen fuel cell aircraft

The lower heating value (LHV) of hydrogen is three times larger than for regular jet fuel, but hydrogen has much lower density at atmospheric sea-level conditions [7, 8]. The hydrogen storage density therefore has to be increased to make it feasible for any type of vehicle. Gaseous hydrogen (GH₂) is commonly used in the automotive sector, where it is compressed to either 350 or 700 bar, with the latter bringing up the density to 39.1 kg/m³ [9]. This is roughly a 20x lower density compared to jet fuel, and will therefore cause unfeasible storage volumes in addition to the large weight penalty of containing a high pressure. Instead, LH₂ is the feasible option for aircraft. LH₂ at atmospheric pressure has a density of 71.9 kg/m³ [7] and a boiling point of around 20 K. This shifts the design challenge from containing a very high pressure to instead preventing heat transfer, as this causes the liquid to boil-off into gas which raises the pressure. If pressure increases to the design limits of the tank, the internal energy must be decreased. This is done by either ventilating gas, or by rejecting heat via a cooling system. At the same time, the tank mass must be kept to a minimum. The insulation system therefore has to be light, and because of this it commonly consists of low density foam, or multiple radiation shields contained in a vacuum jacket, also known as multi-layer insulation (MLI). For regional hydrogen aircraft, the tank's gravimetric index (GI) must exceed 45% to not carry any range penalty compared to its kerosene counterpart [10]. The tanks can then either be placed internal to the aircraft structure, either as an integral or non-integral part of the structure, or externally.

Proton-exchange membrane fuel cell (PEMFC) technology in conjunction with LH₂ storage is currently the most viable option for electric flight, as today's battery technology offers insufficient specific energy and is unsuitable for flight ranges in excess of 230+ NM [11]. The fuel cell stack is on the other hand quite complex, and requires auxiliary components to maintain the conversion process, so called balance-of-plant (BoP) components. An aircraft design strives to maintain low drag and weight, which can be hard to achieve with a fuel cell propulsion system. Firstly, regardless of stack operating pressure, compression of the incoming air has to be provided due to changes in altitude. This is usually performed by an electrically driven compressor, which is a parasitic power loss. Secondly, current fuel cell technology is limited to internal temperatures around 80 °C [10], which makes the process of rejecting megawatts of heat very difficult. This causes the required surface area of the heat-exchangers to be very large, which can carry a severe drag penalty.

There are currently several aircraft manufacturers developing regional electric aircraft driven by hydrogen fuel cells. Universal Hydrogen successfully tested a Dash 8-300 turboprop aircraft retrofitted with an electric fuel cell system [12]. The company is working on conversion kits for the previously mentioned aircraft as well as similar types such as the ATR72. The LH₂ tanks will be located behind the cabin, and the fuel cell stacks contained in the motor nacelles.

3. SUAVE

The Stanford University Aerospace Vehicle Environment, or SUAVE for short, is an open-source software made for conceptual design studies of both conventional and unconventional aircraft designs.

SUAVE is built to handle varying levels of model fidelity, ranging from lower-fidelity classical correlation based methods, common in weight and parasitic drag estimations, up to higher-fidelity computational fluid dynamics methods to estimate lifting performance. This multi-fidelity allows the user to, at an acceptable computational cost, examine certain systems and processes in greater detail, without sacrificing the full system perspective.

Conceptually designing fuel cell hydrogen aircraft poses particular challenges. Firstly, it is generally more tedious to estimate the fuel cell system's fuel consumption during different flight regimes compared to more conventional powerplants, due to the fuel cell's highly dynamic BoP power consumption. Secondly, the LH₂ is sensitive to boil-off caused by external heat transfer. In order to design a suitable tank for a given aircraft and mission, the tank's internal pressure and ventilation of fuel has to be accounted for while evaluating the mission performance. With these considerations in mind, an extension of the existing SUAVE code is necessary to be able to size a representative propulsion system and cryogenic storage, as well as to study the impact of both the consumed and ventilated fuel on the overall mission performance.

4. Design methods

The conceptual design implementation consists of methods for sizing the fuel cell propulsion system and hydrogen storage, as well as airframe resizing. The individual sizing functions are applicable to any aircraft type, but can be combined to form a tailored sizing workflow for a particular application. The method described here concerns redesigns of existing turboprop aircraft, where the propulsion system is swapped and the fuselage and wings resized to accommodate the added volume and weight brought on by the new propulsion.

The implemented sizing workflow consists of three major steps:

1. Definition of the baseline aircraft to be redesigned

First, the routine requires the user to parameterize the baseline aircraft, which will be subjected to the redesign. This includes defining the geometry of the fuselage, wing and empennage, as well as defining take-off, zero-fuel and empty weights. The baseline propulsion system is not modeled, other than estimating its weight. Once the baseline aircraft is defined, a weight breakdown is performed using weight correlation methods, in this case the "New SUAVE" weight method [5]. The weight breakdown of the baseline design is used for the resizing step where the weight and centre-of-gravity (CoG) are updated. Lastly, the aircraft's high-lift system is configured to ensure correct reference speeds.

2. Definition of the hydrogen fuel cell propulsion system

The next step is to define the new fuel cell electric energy network. For each nacelle, a propeller, electrical motor and fuel cell stack is defined and built. After this the propeller and electrical motor are designed, using the available design methods in SUAVE [5]. Finally, the fuel cell stack and its auxiliary balance-of-plant (BoP) components are sized.

The hydrogen storage design is driven by the required fuel volume, number of tanks, insulation design, pressure loading and geometric constraints such as fuselage internal volume. The method

structurally sizes the tank walls in accordance with the internal pressure load case (set by the ventilation pressure) and outside conditions.

3. Resizing of the baseline aircraft weight and geometry

With the baseline aircraft and the new propulsion system defined, the actual aircraft resizing can take place. With the total fuel volume set, by either user or optimization input, the tanks are sized. This sets the amount that the fuselage will be extended by. This increases the fuselage wetted area and translates the empennage rearward. The design then enters an iterative scheme where the geometric changes in the airframe causes the total aircraft weight to increase, and the increase in weight then changes the geometry. This is repeated until the total weight and centre-of-gravity (CoG) position of the aircraft have converged. If a target power-to-weight ratio is set, a propulsion resizing is performed in each iteration.

4.1 Hydrogen storage design

A method for mechanically sizing non-integral MLI LH₂ tanks has been implemented into SUAVE. The tank dimensions are limited by the fuselage internal diameter, and is of spherical or cylindrical shape depending on the required fuel volume. It is assumed that 92% of the fuselage diameter is usable. The design routine will output a spherical tank if possible, as less surface area per volume will result in superior heat transfer performance compared to other shapes. If a spherical tank does not produce the required internal volume, a cylindrical section between the hemispherical end-caps is added. The tank walls can be made out of steel or aluminium alloys appropriate for cryogenic conditions.

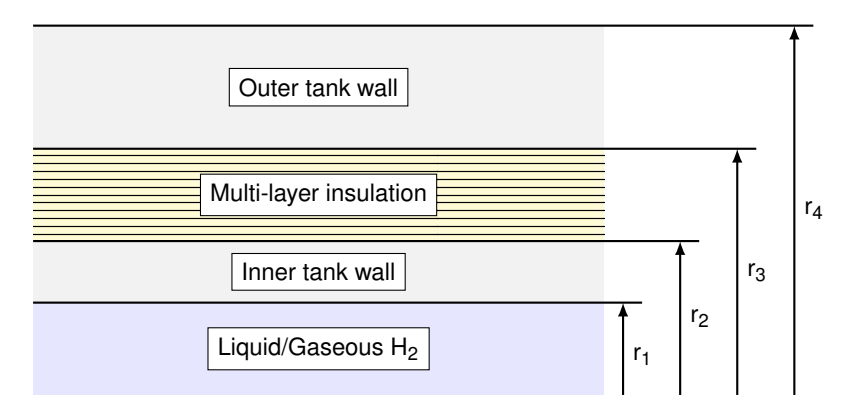


Figure 1 – Illustrative cross-section of an MLI tank.

The MLI requires the tank to consist of an inner and an outer tank wall, with a near-vacuum contained in-between (see Figure 1). The distance between the inner and outer walls are set by the number of insulation layers N_{MLI} and the layer density N_t

$$t_{MLI} = N_{MLI}/N_t \tag{1}$$

The inner wall is designed to withstand internal pressure loading caused by the pressure difference between the ventilation pressure p_{max} and the vacuum jacket pressure p_{MLI} . The inner wall pressure loading becomes

$$\Delta p_{inner} = p_{max} - p_{MLI} \tag{2}$$

As with any pressure vessel design extra safety margin has to be added to the load case. To account for imperfect ventilation valves a 10% increase of p_{max} is included in accordance with [13], and finally

a factor of two is added to account for dynamic loads in-flight

$$p_{design,inner} = 2 \cdot (1.1\Delta p_{inner}) \tag{3}$$

The wall thickness of the inner shell can then be found using equations for welded pressure vessels [14], where K defines the sphericity of the endcaps, e_w a weld weakness factor and SF_{inner} a desired yield safety factor.

$$t_{w,inner} = r_2 - r_1 = \begin{cases} \frac{2 \cdot p_{design,inner} \cdot r_2 \cdot K}{2 \cdot (\sigma_y / SF_{inner}) \cdot e_w - 2 \cdot p_{design,inner} \cdot (K - 0.1)} & \text{(spherical)} \\ \frac{2 \cdot p_{design,inner} \cdot r_2}{2 \cdot (\sigma_y / SF_{inner}) \cdot e_w - 0.8 \cdot p_{design,inner}} & \text{(cylindrical)} \end{cases}$$

The external wall is designed to withstand buckling caused by the external pressure in the unpressurized part of the fuselage. The worst-case loading occurs at sea-level pressure $p_{\infty,max}$. The outer wall pressure loading becomes

$$\Delta p_{outer} = p_{\infty,max} - p_{MLI} \tag{5}$$

and after accounting for dynamic loading the design pressure for the outer tank wall becomes

$$p_{design,outer} = 2 \cdot \Delta p_{outer} \tag{6}$$

The thickness of the outer shell is then found using equations for bucking of thin shells [15]

$$t_{w,outer} = r_4 - r_3 = \begin{cases} \sqrt{\frac{p_{design,outer} \cdot SF_{outer} \cdot r_4^2}{0.365E}} & \text{(spherical)} \\ \left[\frac{\left(p_{design,outer} \cdot SF_{outer} \cdot L_{cyl} \cdot r_4^3 / (0.807E)\right)^4}{(1/(1-v^2))^3} \right]^{1/10} & \text{(cylindrical)} \end{cases}$$
(7)

where L_{cyl} is the length of the cylindrical segment and SF_{outer} the safety factor on the critical buckling pressure.

With the wall and insulation thickness known, the combined total tank weight is calculated using the specified tank wall material density and a layer specific area density $(kg \cdot m^{-2}/layer)$ for the MLI (derived from the "45 layer standard MLI" covered in [16]). Table 1 details the parameters used in the tank design.

Moreover, the routine calculates the initial fuel mass and liquid-gas fraction available at mission start, which is a function of desired gas ullage and the fill and ventilation pressures. Considering two tanks with the same fill pressure and desired gas ullage, the tank with a higher ventilation pressure will have less total fuel mass and a larger fraction of gas at the filling pressure.

Lastly, a key performance metric for tank design is the gravimetric index (GI), which is defined as

$$GI = \frac{m_{fuel}}{m_{fuel} + m_{tank}} \tag{8}$$

Table 1 – Structural parameters and material properties used in the tank design.

Parameter	Value	Description
σ_{y}	228 MPa	Yield strength (AL5083 [17])
\vec{E}	71 GPa	Young's modulus (AL5083 [17])
e_w	0.8	Weld weakness factor
K	0.5	Sphericity of end caps
SF_{inner}	2	Safety factor on yield strength
SF_{outer}	2.5	Safety factor on critical buckling pressure
MLI density	0.0272 kg · m ⁻² / layer	Layer specific area density
N_t	20 layers/cm	MLI layer density

4.2 Fuel cell propulsion design

The fuel cell propulsion system in each nacelle consists of multiple fuel cell stacks connected in a multi-stack configuration to produce a desired voltage, power and size. The multi-stack system also requires balance-of-plant (BoP) components such as heat-exchangers, coolant pumps and air compressors.

4.2.1 Multi-stack design

In the multi-stack, individual fuel cells are connected in series to develop the desired system voltage. Multiple stacks are then connected in parallel to raise the power to the desired level. For an input current density i [A/cm²], a single fuel cell's voltage (polarization curve) is modeled according to [18]

$$V_{cell} = E_r - \eta_{act} - \eta_{ohm} - \eta_{conc}$$

$$\eta_{act} = [a_A + b_A \log(i + i_{leak})] + [a_C + b_C \log(i + i_{leak})]$$

$$\eta_{ohm} = iASR_{\Omega}$$

$$\eta_{conc} = C \log \frac{i_L}{i_L - (i + i_{leak})}$$
(9)

where E_r is the reversible cell voltage, η_{act} activation losses, η_{ohm} ohmic or resistive losses and η_{conc} concentration losses due to mass transport. The activation loss terms are defined by

$$a_A = -\frac{RT_{FC}}{\alpha_A n_A F} \log i_{0A}, \qquad b_A = \frac{RT_{FC}}{\alpha_A n_A F}, \qquad a_C = -\frac{RT_{FC}}{\alpha_C n_C F} \log i_{0C}, \qquad b_C = \frac{RT_{FC}}{\alpha_C n_C F}$$
(10)

where R is the universal gas constant and F Faraday's constant. For the remaining model parameters, see Table 2.

The cell's efficiency is defined as

$$\eta_{FC} = \frac{V_{cell}}{F_{c}} \tag{11}$$

where E_h is the voltage potential corresponding to the higher heating value (HHV) of hydrogen.

The first step in the sizing is to choose the design point on the polarization curve at which the stacks are sized at. The power produced by a single fuel cell is defined as

$$P_{cell} = p_{cell} A_{cell} = (iV_{cell}) A_{cell}$$
(12)

where p_{cell} is the cell's power density [W/cm²] and A_{cell} [cm²] the cell active area. The total power produced by the multi-stack is calculated as

$$P = N_{stacks}P_{stack} = N_{stacks}(N_{cells.stack}P_{cell})$$
(13)

where N_{stacks} are the number of stacks connected in parallell and $N_{cells,stack}$ the number of cells connected in series per stack.

To begin the sizing, the cell design point (denoted as D) and maximum system voltage for the multi-stack are chosen. The number of cells per stack then becomes

$$N_{cells,stack} = \lceil \frac{V_D}{V_{D,cell}} \rceil \tag{14}$$

where V_D is the total voltage produced by the multi-stack at maximum load. The total number of cells in the multi-stack is then simply

$$N_{cells} = N_{stacks} N_{cells.stack} \tag{15}$$

The active area of each cell is then determined by the number of cells and power output at maximum load

$$A_{cell} = \lceil \frac{P_D}{P_{D,cell} N_{cells}} \rceil \tag{16}$$

It is now possible to determine the geometry and weight of the multi-stack. The total length, width and depth of the system will depend on the chosen stack configuration and placement of balance-of-plant (BoP) components. For a given equivalent cell thickness t_{cell} , the length per stack in the multi-stack becomes

$$L_{stack} = N_{cells,stack}t_{cell} \tag{17}$$

By default the BoP is located behind the multi-stack and assumed to extend the combined assembly in length by $0.5L_{stack}$.

The volume per stack is then

$$V_{stack} = N_{cells,stack} A_{cell} t_{cell} \tag{18}$$

and finally the mass per stack is defined using an equivalent cell density ρ_{cell} and a stack porosity coefficient ϕ_{stack}

$$m_{stack} = V_{stack} \rho_{cell} \phi_{cell} \tag{19}$$

Finally, the total mass of the system is the combined mass of the stacks and BoP components

$$m_{FC} = m_{multi-stack} + m_{BoP} = N_{stacks} m_{stack} + m_{BoP}$$
 (20)

Table 2 – Fuel cell model parameters obtained from [19] for a modern fuel cell.

Parameter	Value
E_r	1.1782 V
E_h	1.472 V
i_{0C}	0.0001
α_C	0.22
i_{0A}	0.1
$\alpha_{\!\scriptscriptstyle A}$	0.5
ASR_{Ω}	$0.04~\Omega~\text{cm}^2$
i_L	2.45 A/cm ²
<i>i</i> _{leak} 0.30 A/cn	

Parameter	Value
С	0.035 V
n_A	2
n_C	4
T_{FC}	353.15 K
p_{FC}	2.5 bar
t_{cell}	0.001381 m
ϕ_{stack}	1
$ ho_{cell}$	2854 kg/m ³

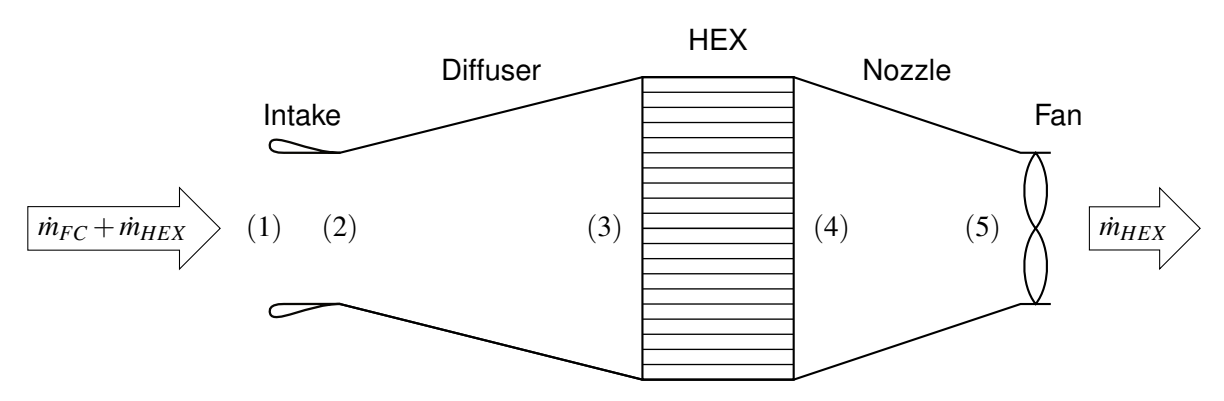


Figure 2 – Illustration of cooling duct.

4.2.2 Cooling system design

The cooling system is comprised of a electric coolant pump and a cooling duct (CD) in the nacelle, in which an air-to-liquid heat-exchanger (HEX) and a puller-fan is located. The cooling duct consists of a ram-air intake, a diverging diffuser duct and a converging nozzle, as illustrated in Figure 2.

The ram-air scoop intake is designed according to the procedures outlined in [20]. At the desired sizing design condition D, the total mass flow of air entering the cooling duct is

$$\dot{m}_{D,CD} = \dot{m}_{D,FC,air,in} + \dot{m}_{D,HEX,air} \tag{21}$$

where $\dot{m}_{D,FC,air}$ is the mass flow of the fuel cell system's inlet air at design power, and $\dot{m}_{D,HEX,air}$ the required amount of air through the heat-exchanger in order to reject the heat produced at design power.

The required intake area is then

$$A_1 = \frac{\dot{m}_{D,CD}}{\rho_{\infty} \nu_{\infty}} \tag{22}$$

where ρ_{∞} and ν_{∞} are the freestream density and airspeed. As the intake will be located in the leading edge of the nacelle, it is assumed there is no blockage caused by boundary layer build-up. Subsequently, the blockage compensation described [20] is skipped. The intake dimensions are dictated by the required intake area and the intake aspect ratio AS.

Next, the planar diffuser section is designed. The performance of the diffuser is calculated using the pressure recovery map correlations by Pittaluga [21]. In this, the coefficient c_p^* refers to a optimal pressure recovery locus at a constant length-to-width ratio. A diffuser wall-divergence angle of $\theta=8^\circ$ is assumed for the entire performance map c_p^* locus. The entry area of the diffuser is equal to the intake area $A_2=A_1$, and the diffuser exit area is found using the diffuser area ratio AR. The length of the diffuser duct is then simply

$$l_{diff} = \frac{w_2(AR - 1)}{2tan(\theta)} \tag{23}$$

The HEX dimensions L_y and L_z are set by the diffuser exit area, while its length in the air's streamwise direction L_x is driven by the cooling requirement. For a required heat rejection rate at the design point, Q_D , the required air mass flow through the HEX is

$$\dot{m}_{D,HEX,air} = \frac{Q_D}{c_{D,3}\Delta T_{D,air}} \tag{24}$$

where c_{p_3} is the diffuser exit specific heat and $\Delta T_{D,air}$ the temperature rise of the air through the HEX at the sizing point. As the temperature rise dictates the required massflow, which affects the

total pressure losses both in the cooling duct and inside the HEX itself, $\Delta T_{D,air}$ becomes a design parameter in the cooling system sizing. Similarly, the coolant mass flow at the sizing point is

$$\dot{m}_{D,HEX,cool} = \frac{Q_D}{c_{p_{cool}} \Delta T_{D,cool}}$$
 (25)

With the inlet conditions for the air and coolant set, an appropriate HEX design is generated using the in-house software GenHEX [22]. The software uses a generalized design formulation and computes the performance using a set of correlations together with the $\varepsilon-NTU$ method. The length L_x and non-dimensional quantities σ_r , α_r and χ are unknown geometric parameters and are solved via optimization to satisfy the cooling requirement.

Finally, the converging nozzle section is sized. The duct convergence angle is quite aggressive in order to reduce the overall cooling duct length, as it is assumed that little to no pressure losses occurs. The outlet area is sized to bring the pressure back to ambient. It also dictates the puller-fan diameter.

For the full set of geometric relations in the cooling duct, see Table 3.

Table 3 – Cooling duct geometric relations.

Station 1	Station 2	Station 3	Station 4	Station 5
$A_1 = \frac{\dot{m}_{D,CD}}{\rho_{\infty} v_{\infty}}$	$A_2 = A_1$	$A_3 = AR \cdot A_2$	$A_4 = A_3$	$A_5 = AR_{nozzle}A_4$
$b_1 = d_{1sc} = \sqrt{A_1 \cdot AS}$	$b_2 = b_1$	$b_3 = b_2 = L_z$	$b_4 = b_3$	$b_5 = b_4$
$w_1 = A_1/b_1$	$w_2 = w_1$	$w_3 = A_3/b_3 = L_y$	$w_4 = w_3 = L_y$	$w_5 = A_5/b_5$

4.2.3 Combined sizing procedure

The total power output of the fuel cell system (per nacelle) has to be able to provide the wanted propulsive power and be able to drive BoP components such as the coolant pump, cooling fan and air compressor. The combined sizing problem is then simply to find a factor k_D

$$P_D = P_{D,prop} + P_{D,BoP} = P_{D,prop} + (P_{D,comp} + P_{D,pump} + P_{D,fan} - P_{D,turb}) = k_D P_{D,prop}$$
(26)

at which the heat rejection requirement is

$$Q_{D} = Q_{D,FC} + Q_{D,motor} - Q_{D,air}$$

$$= \left(\frac{1}{\eta_{FC}} - 1\right) k_{D} P_{D,prop} + \left(\frac{1}{\eta_{motor}} - 1\right) P_{D,prop} - c_{p,air,stack} \dot{m}_{D,FC,air,out} (T_{stack} - T_{\infty})$$
(27)

where the first term $(Q_{D,FC})$ is the heat produced by the multi-stack, the second term $(Q_{D,motor})$ the heat produced by the motor and the third term $(Q_{D,air})$ the heat rejected via the fuel cell exhaust. The exhaust mass flow of the fuel cell system is calculated according to [19]

$$\dot{m}_{D,FC,air,out} = \frac{S_O}{NF} \left(\frac{f_A m_A}{x_O} - m_O \right) \frac{k_D P_{D,prop}}{V_{D,cell}}$$
(28)

To ensure the fuel cell system is able to produce enough power to overcome pressure losses in caused by the cooling system, and to ensure the cooling system is able to reject enough heat, k_D is solved for using the routine below:

- 1. Set $k_{D,guess}$
- 2. Given $k_{D,guess}$, calculate required heat rejection and size cooling duct and HEX

- 3. Run the fuel cell sizing code, where the BoP components are sized to cope with the losses produced by the cooling duct and HEX. This will output $k_{D,actual}$
- 4. If $k_{D,guess} = k_{D,actual}$, the system sizing is converged, otherwise update guess

As there are several solutions in the resulting design space which satisfy the cooling requirement, the HEX, cooling duct and multi-stack design are preferably optimized together to minimize overall aircraft drag.

4.3 Aircraft resizing

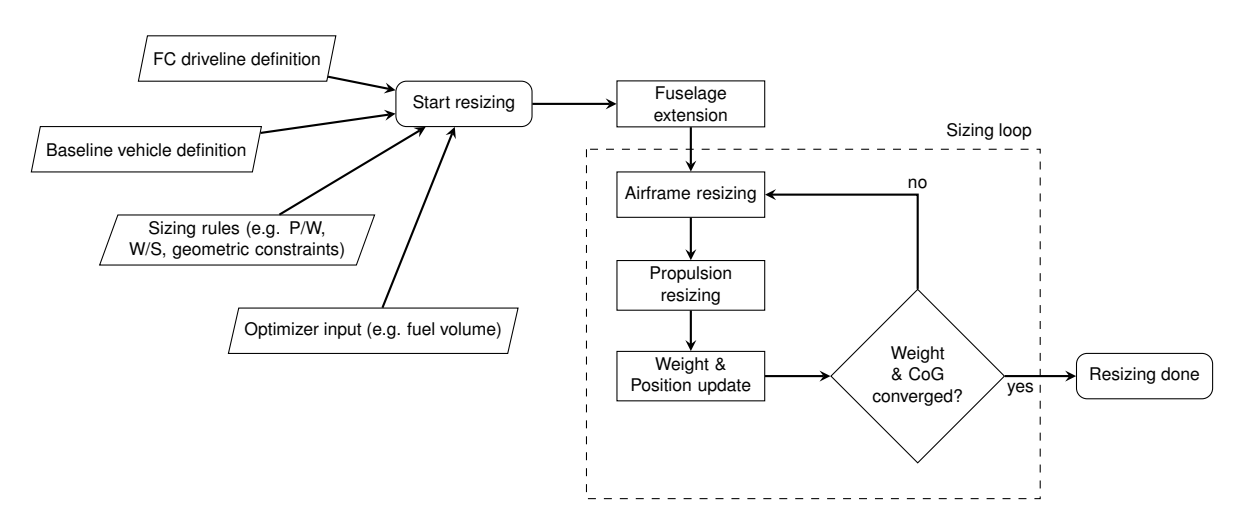


Figure 3 – Iterative resizing scheme.

The resizing routine estimates the change in aircraft geometry, weight and centre-of-gravity brought on by changing the propulsion system, and predicts the aerodynamic changes brought on by reshaping the aircraft. To initialize the resizing, the weight breakdown and geometric parameters of the baseline aircraft are brought in. Next, the fuselage is stretched by adding a section between the cabin and empennage, in order to fit the hydrogen tanks. The horizontal and vertical stabilizers are then moved rearward an amount equal to the stretch.

After the initialization, the actual resizing loop is started. The first step is to resize the wing to match a target wing loading. By default the wing is scaled uniformly to maintain the wing's aspect ratio (*AR*). If wanted, the wing loading and aspect ratio can be treated as optimization inputs. After the wing has been scaled, the horizontal and vertical stabilizers can be sized. With the tail volume coefficients set and moment-arm distances known, the resulting tail areas are calculated. By default the original volume coefficients are kept in order to maintain the stability properties of the baseline aircraft. The next step is then to resize the propulsion system in order to achieve a target power-to-weight (P/W) ratio (by default it conserves the original P/W of the baseline aircraft). As the design point for the cells, system voltage and number of stacks are already set, only cell areas are changed to increase the power. BoP components are resized as well, keeping their previously set design point.

With the airframe and propulsion system resized, it is then possible to update the component weights using empirical weight methods (by default the "New SUAVE" method [6]). The weight of the propulsion system takes into account the multi-stack itself, the BoP components, electrical motor and propeller. The nacelle weight depends on the diameter and length of the fuel cell system.

The maximum zero-fuel weight (MZFW) of the baseline aircraft is updated according to

$$MZFW = MZFW_{base} - (m_{propulsion} + m_{fuselage} + m_{wing} + m_{empennage})_{base} + (m_{propulsion} + m_{fuselage} + m_{wing} + m_{empennage})_{resized}$$
(29)

and the new maximum take-off weight (MTOW) is found by adding the weight of the fuel, which is determined outside the resizing routine by the user or the SUAVE optimizer

$$MTOW = MZFW + m_{fuel,total} (30)$$

The longitudinal CoG is updated in each sizing iteration and follows a set of sizing rules. The rules for the individual CoG's of the wing, fuselage and tail assembly are the default SUAVE implementation [6], which are based on classic text-book estimations.

As the stretching of the fuselage only concerns the aft space behind the cabin, the cabin furnishing, passengers and cargo remain unchanged in terms CoG location. The nose and tail cone assemblies do not change in size. The fuselage CoG is at 45% of the total length. The stretching of the fuselage moves the tail assemblies rearward, and depending on their updated weight they can impact the total aircraft CoG.

The wing's CoG is located at 30% of its mean-aerodynamic-chord (MAC). It is then repositioned relative to the total aircraft CoG in each sizing iteration in order to achieve a desired total CoG. This repositioning changes the lever-arm distance to the tail sections and therefore has an effect on their size.

For the propulsion system CoG location, the weight and location of the fuel and tanks has a significant effect, as it is located in a space behind the cabin aft bulkhead. By default the identical tanks are placed behind one another in the fuselage, and their combined CoG is assumed to be located at 50% of the combined length. The fuel cell multi-stack and the BoP components are assumed to have their CoG at 50% of their respective lengths.

The total aircraft CoG is updated according to (in this case for the MZFW)

$$CoG = \frac{(CoG \cdot MZFW)_{base} + \sum_{n=1}^{k} \left[(CoG_n \cdot m_n)_{resized} - (CoG_n \cdot m_n)_{base} \right]}{MZFW_{base} + \sum_{n=1}^{k} \left[(m_n)_{resized} - (m_n)_{base} \right]}$$
(31)

where n is one of the components being resized.

The resizing is considered to have converged when the difference between the current and previous iteration's MZFW and longitudinal CoG both are below a set tolerance.

5. Dynamic models

5.1 Hydrogen boil-off

The thermodynamic state of the fuel is calculated for each time step during the mission solving and has a direct effect on mission performance. The main state variable of interest is the pressure inside the tank as pressure should not drop below the fill pressure, and not exceed the design limits of the tank design. Using the control volume approach presented in [23], the homogeneous pressure inside the tank varies over time according to

$$\frac{dp}{dt} = 2\frac{\Phi}{V} \left[1.3Q_{MLI} - \Delta h \left(\dot{m}_{gas} + \rho^* \left(\dot{m}_{gas} + \dot{m}_{liquid} \right) \right) \right]$$
(32)

where

$$p^* = \frac{\rho_{gas}}{\rho_{gas} + \rho_{liquid}} \tag{33}$$

and the energy derivative is defined as

$$\Phi = \frac{1}{\rho \frac{\partial u}{\partial p}} \tag{34}$$

The state variables of the two hydrogen phases are calculated using the thermodynamic library Cool-Prop [24].

The factor of two in Equation 32 is to compensate for a lack of fluid stratification in the model [23] and the heat transfer rate Q_{MLI} through the tank walls and insulation is increased by 30% in accordance with [13] to account for heat transfer via components such as pipes and structural attachments. The mass flow rates in \dot{m}_{gas} and \dot{m}_{liquid} relate to the ventilation of gaseous hydrogen and liquid fuel consumption to power the fuel cell stacks. If the pressure reaches the limit of the tank design, the internal energy must be decreased. This is achieved by ventilating gas. It should be observed that the fuel flow also will lower the pressure, and can in cases with too little heat transfer input and high fuel flow rates cause the pressure to drop below the fill pressure. To prevent structural failure and the risk of the external atmosphere entering the tank, the pressure must never drop below the set fill pressure. To maintain a high enough tank pressure, the insulation must be designed to have the right amount of thermal resistance. The ventilation is dynamically controlled during the mission solving routine.

The heat transfer rate Q_{MLI} in Equation 32 is solved by accounting for external and internal convection for both the gas and liquid, as well as radiative heat transfer from the tank exterior surface. The convective heat transfer is modeled through a Nusselt-number correlation for a vertical flat plate, with the length set to the tank diameter [25]

$$\overline{Nu} = \left[0.825 + \frac{0.387Ra^{1/6}}{(1 + (0.492/Pr)^{9/16})^{8/27}} \right]^2$$
 (35)

As the tank wall material is highly conductive, this thermal resistance is neglected. The heat flux through the MLI is modeled by an empirical model that evaluates all layers in bulk. The MLI model is an adaptation [26] of the semi-empirical Lockheed model [27] and relies on experimentally determined model parameters (see Table 4)

$$q_{MLI} = C_1 N_t^{C_2} \frac{(T_H + T_C)(T_H - T_C)}{2(N_{MLI} + 1)} + C_3 \varepsilon \frac{T_H^{4.67} - T_C^{4.67}}{N_{MLI}} + C_g \frac{p_{MLI}}{N_{MLI}} (T_H^{n_g} - T_C^{n_g})$$
(36)

where T_H and T_C are the hot and cold surface temperatures, respectively.

The resulting rate of heat transfer into the tank is then calculated by numerically solving for Q_{MLI}

$$Q_{conv,air} + Q_{rad} = Q_{MLI}$$

$$Q_{conv,gas} + Q_{conv,liq} = Q_{MLI}$$
(37)

Table 4 – Model parameters for the MLI system ("DAM/Tissuglas" [26]) and chosen vacuum-level.

Parameter	Value
C_1	$4.43 \cdot 10^{-11}$
C_2	3.91
C_3	$8.03 \cdot 10^{-10}$
C_g	$1.46 \cdot 10^4$
n_g	0.53
p_{MLI}	1 mBar

5.2 Cooling duct

At a given time in the mission, the total pressure inlet condition for the fuel cell system's air compressor and HEX is

$$p_{tot,3} = \Pi_{inlet} \Pi_{diffuser} p_{tot,1} \tag{38}$$

where $p_{tot,1} = p_{tot,\infty} + \Delta p_{tot,fan}$ is the total pressure in at the intake face produced by the forward-flight and the cooling fan, Π_{inlet} and $\Pi_{diffuser}$ the total pressure ratios across the inlet and diffuser respectively.

The total pressure loss experienced in the scoop inlet follows the methods described in [20]. The boundary layer height is set to $\delta/h=0.2$ and is assumed for both upper and lower lips of the scoop. Additional pressure losses when the inlet is not running at full mass flow is assumed to be zero, due to being located in the leading edge of the nacelle. The total pressure ratio then only becomes a function of the freestream Mach number (correlation valid in 0.2 < M < 1.0).

The losses produced in the scoop inlet then enters the throat of the planar diffuser. Using the correlation proposed by [21], the optimal pressure recovery locus for a constant length is defined as

$$c_p^* = g_1 \cdot g_2 \left[1 - \frac{1.03 \cdot (1 - B_2)^2}{\overline{AR}^2 \left(1 - 0.820 \cdot \overline{AR}^{0.07} B_2^{1/(2\overline{AR} - 1)} \right)^2} \right]$$
 (39)

where \overline{AR} is the diffuser area ratio corrected for boundary layer blockage and B_2 is the percentage of area lost to the blockage (assumed to be 2%). For further details on the remaining model parameters, see [21]. The correlation is valid for inlet conditions in the range of Re > 100000, $0.02 \le B_2 \le 0.12$, $M_2 \le 0.8$, $2 \le AR \le 4$. The flow conditions for this application differ from the correlation and much data on available on diffusers, due to the presence of flow resistance in the diffuser exit. However, no significant effects on the pressure recovery (other than the flow resistance producing a pressure loss itself) are to be expected from this [28].

The total pressure ratio in the diffuser can then be expressed as

$$\Pi_{diffuser} = \frac{p_{tot,3}}{p_{tot,2}} = \frac{\left(p_2 + c_p^* q_2\right) + q_3}{\Pi_{inlet} p_{tot,1}} \tag{40}$$

where the dynamic pressure q_3 in the diffuser exit is calculated by assuming adiabatic compression. The exit speed becomes

$$v_3 = \sqrt{v_2^2 + \left(\frac{2\gamma}{\gamma - 1}\right) \left(\frac{p_2}{\rho_2} - \frac{p_3}{\rho_3}\right)} \tag{41}$$

where

$$\rho_3 = \frac{p_3}{RT_3} = \frac{p_3}{R\left[T_2\left(\frac{p_3}{p_2}\right)^{(\gamma-1)/\gamma}\right]}$$
(42)

Further total pressure losses in the airflow are induced inside the HEX. As the air compressor system is located upstream of the HEX, these losses will only have have an impact on the momentum drag of the cooling duct. The loss of total pressure depends on the HEX geometric parameters, mass flow and the dimensionless friction factor f. GenHEX [22] calculates the friction factor f and Colburn factor f using a correlation-based method fitted to data from [29].

The cooling duct terminates with a contracting nozzle with and a puller-fan in its exit. The calculation of dynamic pressure follows the same principle as in the diffuser, and it is assumed no extra total pressure loss is produced here. The puller-fan is powered when the ambient dynamic pressure is not able to produce the required cooling mass flow. For a given point during the mission, the cooling mass flow deficit is

$$\Delta \dot{m}_{HEX,air} = \frac{Q}{c_{p_{\infty}} \Delta T_{air}} - (\dot{m}_{CD} - \dot{m}_{FC,air,in})$$
(43)

The required volumetric flow produced by the fan is

$$\dot{V}_{fan} = \frac{\dot{m}_{HEX,air}}{\rho_5} \tag{44}$$

The required increase in total pressure at the intake face is then just the cooling mass flow deficit expressed in terms of dynamic pressure

$$\Delta p_{tot,fan} = \frac{0.5}{\rho_1} \left(\frac{\Delta \dot{m}_{HEX,air}}{A_1} \right)^2 \tag{45}$$

Finally, with the speed and pressure mapped throughout the cooling duct, the drag produced by the internal duct flow can be calculated. The loss of total pressure causes the air exiting the duct to be slower than the ambient. The drag force caused by the momentum loss is calculated as

$$D_{cool} = \dot{m}_{CD} \left(v_{\infty} - v_5 \right) \tag{46}$$

5.3 Fuel consumption

During the mission solving, the objective of the fuel cell code is to calculate the total power P produced by the multi-stack (see Equation 26). The air compression system has to boost the static pressure in the cooling duct diffuser exit to the fuel cell stack operating pressure (by default $p_{FC} = 2.5$ bar). The power draw of the compressor system (assuming 75% isentropic efficiency) is

$$P_{comp} = \dot{m}_{FC,air,in} \Delta T_{comp} c_{p,3} = \dot{m}_{FC,air,in} \left[\frac{1}{\eta_{comp}} T_3 \left(\frac{p_{FC}}{p_3} \right)^{\left(\frac{\gamma - 1}{\gamma} - 1 \right)} \right] c_{p,3}$$
(47)

It is assumed that power can be recuperated in the fuel cell exhaust. The power recuperation is (assuming 65% isentropic efficiency)

$$P_{turb} = \dot{m}_{FC,air,out} \Delta T_{comp} c_{p,stack} = \dot{m}_{FC,air,out} \left[\eta_{turb} T_{stack} \left(\frac{p_{\infty}}{p_{FC}} \right)^{\left(\frac{\gamma - 1}{\gamma} - 1 \right)} \right] c_{p,stack}$$
 (48)

The puller-fan is modeled as an ideal fan with an efficiency factor η_{fan}

$$P_{fan} = \frac{\dot{V}_{fan} \Delta p_{tot,fan}}{\eta_{fan}} \tag{49}$$

where \dot{V}_{fan} is the volumetric flow through the fan and $\Delta p_{tot,fan}$ the increase in total pressure inside the cooling duct.

The coolant pump has to overcome the pressure losses inside the HEX and coolant lines and is also modelled as an ideal pump with an efficiency factor

$$P_{pump} = \frac{\dot{V}_{cool} \Delta p_{cool}}{\eta_{pump}} \tag{50}$$

where Δp_{cool} is the total pressure loss in the system.

Finally, the liquid fuel flow in Equation 32 can be calculated according to

$$\dot{m}_{liquid} = P/\left(HHV \cdot \eta_{FC}\right) \tag{51}$$

where HHV is the higher-heating value for hydrogen. The fuel flow rate \dot{m}_{liquid} and gas ventilation rate \dot{m}_{gas} are inputs to SUAVE's mission solver and reduces the vehicle weight according to

$$\dot{m}_{vehicle} = -\left[N_{multi-stacks}\dot{m}_{liquid} + N_{tanks}\dot{m}_{gas}\right] \tag{52}$$

6. Results

6.1 Storage design

A set of tank designs are generated for a redesigned ATR42-600. The tanks are designed with a gas ullage of 3%, and the MLI system has a layer count of $N_{MLI} = 15$.

A study is performed on the effect of total fuel volume on the GI for a fixed fuselage size. The design code outputs spherical shaped tanks if r_4 is less than the available internal diameter, and switches to cylindrical if not. Figure 4 shows the variation of GI for different ventilation pressures, total fuel volumes and number of tanks.

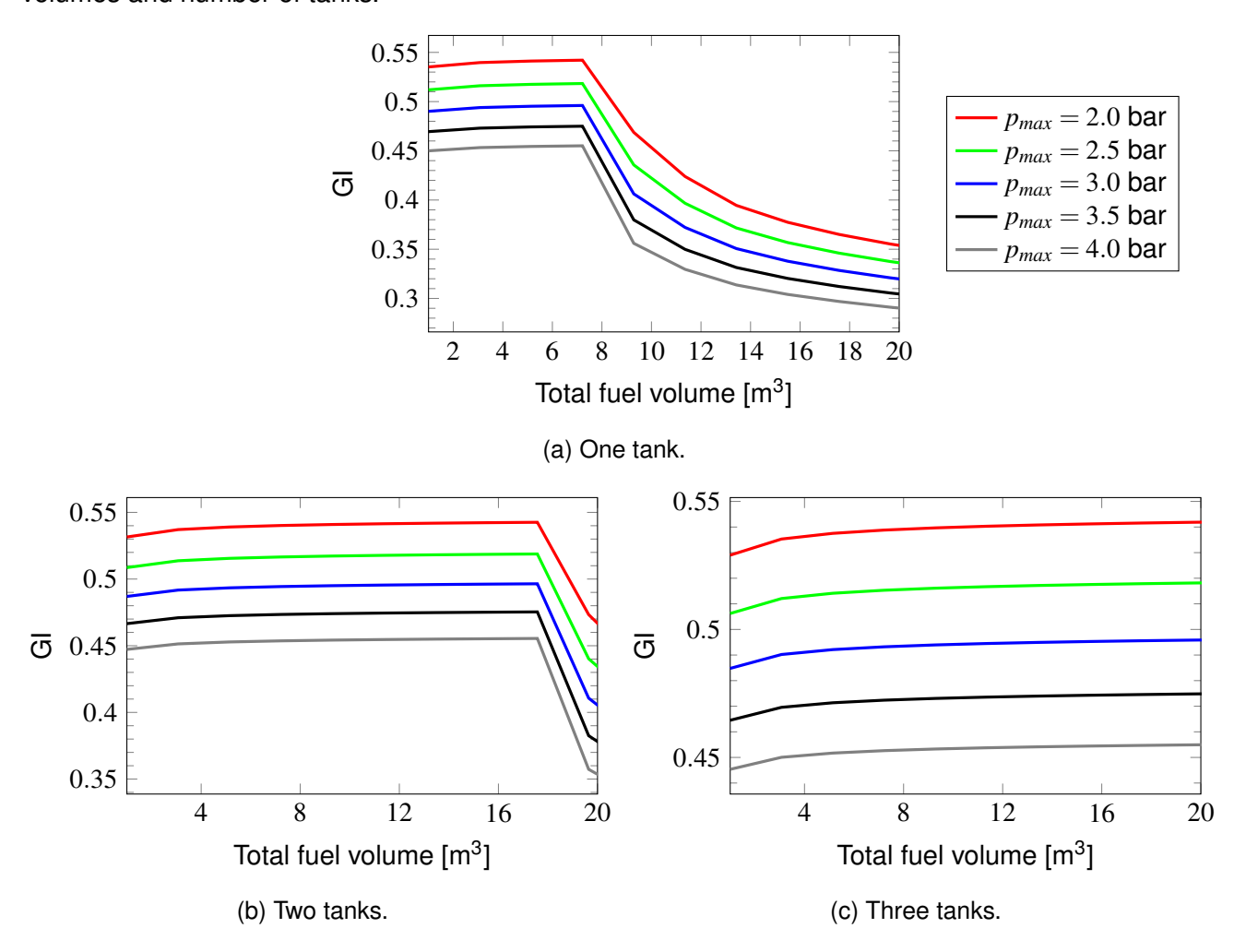


Figure 4 – Variation of GI as function of total fuel volume and ventilation pressure.

It can be observed that if the total fuel volume does not cause the tank diameter to exceed the available space, as few tanks as possible will give the lowest total weight. However, the drop seen in GI when the shape turns cylindrical is possible to delay by splitting the total fuel volume into more tanks.

The disadvantage of splitting the fuel into additional tanks is the increased total heat transfer area. As seen in Figure 5, for a given hot and cold boundary temperature on the insulation system, splitting the fuel increases the heating rate.

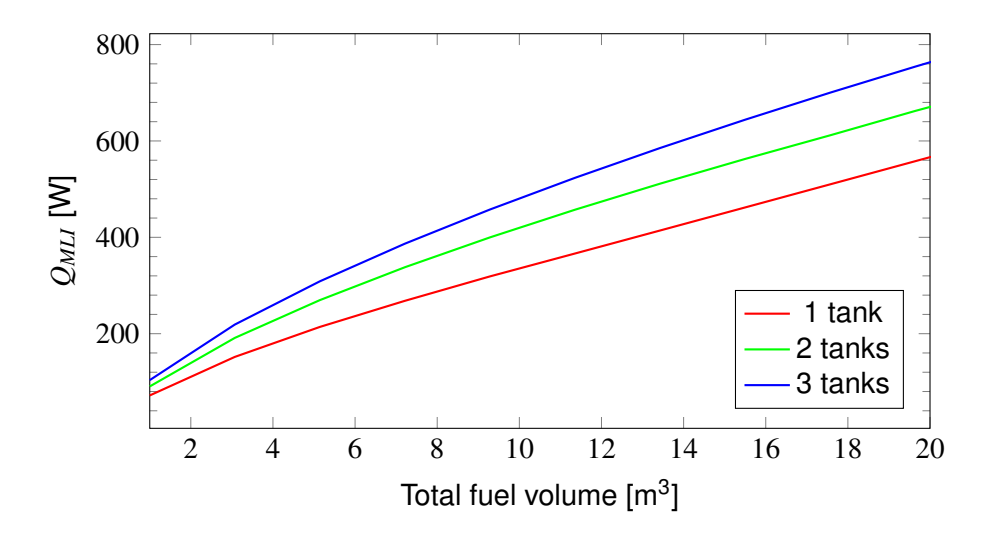


Figure 5 – Variation of total heat transfer rate as function of total fuel volume and number of tanks. $p_{max} = 2.0$ bar, $T_C = 20$ K, $T_H = 273$ K.

6.2 ATR42-600 resizing

An ATR42-600 is redesigned to accommodate 6 m³ of hydrogen with a 3% gas ullage split over two tanks. The inner tank wall is designed for a ventilation pressure $p_{max} = 2$ bar and the insulation system consists of 15 MLI layers. Fuselage diameter, wing aspect ratio and taper, tail volume coefficients, P/W and W/S are unchanged from the baseline. The distance between the nacelle's and wing's leading edges (LE) is also kept.

SUAVE estimates the baseline wing aerodynamic center as 28.3% of MAC, which is then assumed as the baseline total aircraft CoG. The baseline propulsion weight is calculated using the dry weight of the PW127M turboprop and a nacelle weight correlation from [30]

$$m_{propulsion,base} = k_{fudge} N_{props} \left[m_{PW127M,dry} + m_{nacelle,base} = m_{PW127M,dry} + (0.0635 P_{PW127M}) \right]$$
 (53)

where $N_{props} = 2$, $m_{PW127M,dry} = 481$ kg, $P_{PW127M} = 2750$ hp. A fudge factor $k_{fudge} = 1.194$ is added in order to get a matching MZFW when performing the weight breakdown of the baseline aircraft.

The baseline aircraft is compared with the redesign in Tables 5 and 6. Figure 6 illustrates the difference in planform.

The redesign is significantly heavier due to the fuel cell propulsion system, and is longer in order to fit the two hydrogen tanks. A concern when having the tanks located in the aft is the CoG shift during flight. With the assumptions made in this study, the difference in CoG between the MTOW and MZFW condition is 5.5%. Referring to the baseline aircraft's CoG envelope, this amount of shift is within the trim ability. However, because of this the redesign will not exhibit much margin for cargo and passengers shifting around, and is therefore much more limited in its operation.

Interestingly, the tail surfaces have become smaller due to increased moment arm distances. It could be expected to see the wing positioned much further back with having the fuel stored in the aft, but the combined weight of the hydrogen and tanks is a just a fraction of the MTOW. The combined effect of the much heavier propulsion system and a large fuselage extension then causes the fuselage to outgrow the wing repositioning.

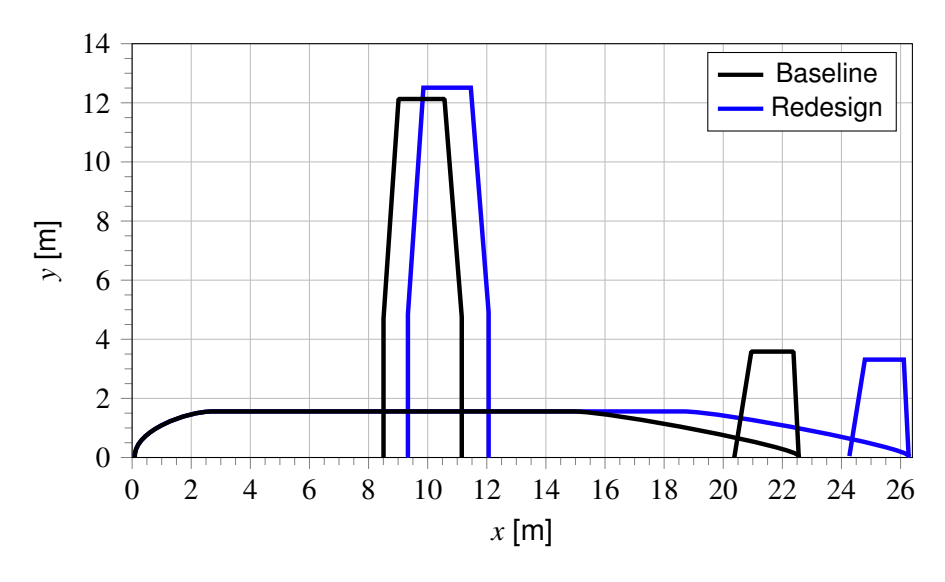


Figure 6 – Baseline and redesigned planform.

Table 5 – Comparison of weights and CoG of resized and baseline aircraft (*estimated value for the baseline aircraft).

Parameter	Baseline	Resized
MTOW	18600.0 kg	19754.7 kg
MZFW	16700.0 kg	19353.5 kg
CoG at MTOW*	28.3% MAC	30.5% MAC
CoG at MZFW *	28.3% MAC	25.0% MAC
Wingloading (at MTOW)	341 kg/m ²	341 kg/m ²
Power-to-weight (at MTOW)	0.192 kW/kg	0.192 kW/kg
Wing weight*	1377.9 kg	1473.9 kg
Fuselage weight*	2460.7 kg	2910.2 kg
Propulsion weight*	1565.7 kg	3430.2 kg
Tank weight (2)	-	342.4 kg
Horizontal stabilizer weight*	296.1 kg	243.8 kg
Vertical stabilizer weight*	287.9 kg	241.2 kg

Table 6 – Comparison of airframe geometry of resized and baseline aircraft (*estimated value for the baseline aircraft).

Parameter	Baseline	Resized
Fuselage length	22.67 m	26.3 m
Fuselage diameter	2.865 m	2.865 m
Wing reference area	54.5 m ²	57.9 m ²
Wing origin (nose to center LE)*	8.6 m	9.5 m
Wing span	24.57 m	25.33 m
Horizontal tail reference area*	11.55 m ²	9.51 m ²
Horizontal tail moment arm*	11.46 m	15.39 m
Vertical tail reference area*	13.97 m ²	11.83 m ²
Vertical tail moment arm*	9.82 m	12.7 m

6.3 Dynamic mission performance

A resized ATR 42-600 with a hydrogen fuel cell driveline and liquid hydrogen storage with a total fuel volume of 7 m³ is simulated performing a 648 NM design mission. The mission is illustrated in Figure 7 and includes reserves in the form of 20 minutes loiter at the destination, a 100 NM alternate

diversion and 30 minutes of loiter for final reserves at the alternate.

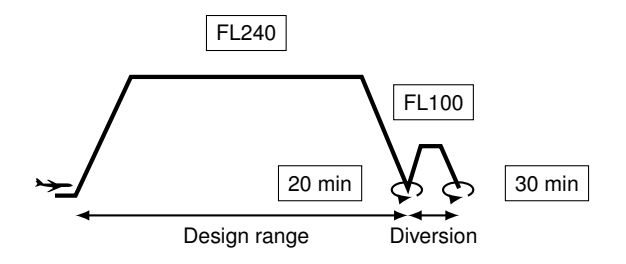


Figure 7 – Design mission.

The dynamic mission performance is illustrated below in Figure 8. The tank has an MLI layer count of 10, which with the chosen layer density corresponds to a total insulation thickness of 5 mm.

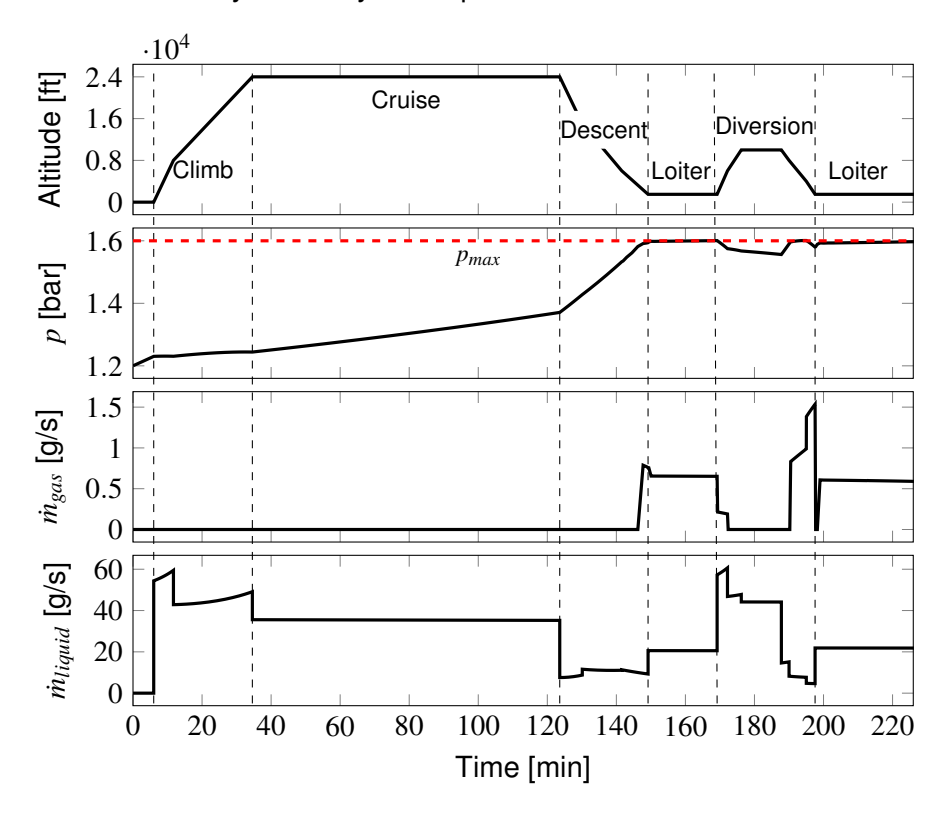


Figure 8 – Variation of altitude, tank pressure, ventilation mass rate and fuel mass rate for during the design mission ($p_{max} = 1.6$ bar, $N_{MLI} = 10$).

The pressure is initially at 1.2 bar, which is the fill pressure, and slowly rises during the climb and cruise portion of the mission. It is observed that the reduction in fuel flow for the cruise segment causes the pressure to rise more rapidly when compared to the previous climb segments. On the contrary, the increased flight altitude will cause less heat transfer, which will counteract the pressure rise. During the descent segments the combination of reduced fuel flow and increased heat transfer causes the pressure to rise rapidly. When the pressure reaches the ventilation pressure $p_{max} = 1.6$ bar, gaseous hydrogen is vented to maintain the pressure level, which is seen in the gas flow rate.

7. Acknowledgements

The Competence Centre TechForH2 is hosted by Chalmers University of Technology and is financially supported by the Swedish Energy Agency (P2021-90268) and the member companies Volvo, Scania, Siemens Energy, GKN Aerospace, PowerCell, Oxeon, RISE, Stena Rederier AB, Johnsson Matthey and Insplorion.

8. Corresponding author

Christian Svensson chrissv@chalmers.se

9. Copyright Statement

The authors confirm that they, and/or their company or organization, hold copyright on all of the original material included in this paper. The authors also confirm that they have obtained permission, from the copyright holder of any third party material included in this paper, to publish it as part of their paper. The authors confirm that they give permission, or have obtained permission from the copyright holder of this paper, for the publication and distribution of this paper as part of the ICAS proceedings or as individual off-prints from the proceedings.

References

- [1] Royal NLR Netherlands Aerospace Centre. Technological developments and radical innovations [online]. 2023. URL: https://www.nlr.org/focus-area/programmes/programme-climate-neutral-aviation/technological-developments-and-radical-innovations/.
- [2] Brandon Graver, Rutherford Dan, and Zheng Sola. CO₂ emissions from commercial aviation: 2013, 2018, and 2019. Technical report, ICCT, 10 2020.
- [3] Liquid hydrogen fuelled aircraft system analysis. Final technical report, Cryoplane project, 2003. URL: https://www.fzt.haw-hamburg.de/pers/Scholz/dglr/hh/text_2004_02_26_Cryoplane.pdf.
- [4] J. Hoelzen, M. Flohr, D. Silberhorn, J. Mangold, A. Bensmann, and R. Hanke-Rauschenbach. H2-powered aviation at airports design and economics of lh2 refueling systems. *Energy Conversion and Management: X*, 14:100206, 2022. URL: https://www.sciencedirect.com/science/article/pii/S2590174522000290, doi:10.1016/j.ecmx.2022.100206.
- [5] Trent Lukaczyk, Andrew D Wendorff, Emilio Botero, Timothy Macdonald, Timothy Momose, Anil Variyar, J. Michael Vegh, Michael Colonno, Thomas D. Economon, Juan J. Alonso, Tarik H Orra, and Carlos Ilario Da Silva. SUAVE: An open-source environment for multi-fidelity conceptual vehicle design.
- [6] A. Wendorff, A. Variyar, C. Ilario, E. Botero, F. Capristan, J. Smart, J. Alonso, L. Kulik, M. Clarke, M. Colonno, M. Kruger, J. M. Vegh, P. Goncalves, R. Erhard, R. Fenrich, T. Orra, T. St. Francis, T. MacDonald, T. Momose, T. Economon, T. Lukaczyk, and W. Maier. SUAVE: An aerospace vehicle environment for designing future aircraft, 2020. URL: https://github.com/suavecode/SUAVE.
- [7] Bent Sorensen and Giuseppe Spazzafumo. *Hydrogen and fuel cells: emerging technologies and applications*. Academic Press, 2018.
- [8] A. Contreras, S. Yiğit, K. Özay, and T.N. Veziroğlu. Hydrogen as aviation fuel: A comparison with hydrocarbon fuels. *International Journal of Hydrogen Energy*, 22(10):1053-1060, 1997. URL: https://www.sciencedirect.com/science/article/pii/S0360319997000086, doi:10.1016/S0360-3199(97)00008-6.
- [9] Zhao Yanxing, Gong Maoqiong, Zhou Yuan, Dong Xueqiang, and Shen Jun. Thermodynamics analysis of hydrogen storage based on compressed gaseous hydrogen, liquid hydrogen and cryo-compressed hydrogen. *International Journal of Hydrogen Energy*, 44:16833–16840, 6 2019. doi:10.1016/j.ijhy dene.2019.04.207.
- [10] Eytan J. Adler and Joaquim R.R.A. Martins. Hydrogen-powered aircraft: Fundamental concepts, key technologies, and environmental impacts. *Progress in Aerospace Sciences*, 141:100922, 2023. Special Issue on Green Aviation. URL: https://www.sciencedirect.com/science/article/pii/S0 376042123000386, doi:10.1016/j.paerosci.2023.100922.
- [11] Jayant Mukhopadhaya and Brandon Graver. Performance analysis of regional electric aircraft. Technical report, ICCT, 7 2022.
- [12] Universal Hydrogen. Universal hydrogen successfully completes first flight of hydrogen regional airliner, 2023. URL: https://hydrogen.aero/press-releases/universal-hydrogen-successfully-completes-first-flight-of-hydrogen-regional-airliner/.
- [13] G D Brewer. Hydrogen Aircraft Technology. CRC Press, 1991.
- [14] Randall F Barron. *Cryogenic Systems*. Monographs on Cryogenics. Oxford University Press, New York, NY, 2 edition, June 1985.

MODELLING HYDROGEN FUEL CELL AIRCRAFT IN SUAVE

- [15] Warren C Young, Richard G Budynas, and Ali Sadegh. *Roark's Formulas for Stress and Strain*. McGraw-Hill Professional, New York, NY, 8 edition, December 2011.
- [16] L. J. Hastings, A. Hedayat, and T.M. Brown. Analytical modeling and test correlation of variable density multilayer insulation for cryogenic storage. Technical Memorandum NASA/TM-2004-213175, NASA, 2004.
- [17] Aerospace Specification Metals. Aluminum 5083-h116; 5083-h321 [online]. 2023. accessed 2023-11-19. URL: https://asm.matweb.com/search/SpecificMaterial.asp?bassnum=ma5083h116.
- [18] Ryan O'Hayre, Suk-Won Cha, Whitney Colella, and Fritz B Prinz. *Fuel Cell Fundamentals*. John Wiley & Sons, Nashville, TN, 3 edition, April 2016.
- [19] Anubhav Datta. PEM fuel cell model for conceptual design of hydrogen eVTOL aircraft. Contractor Report NASA/CR-2021-0000284, NASA, 2021.
- [20] Drag and pressure recovery characteristics of auxiliary air inlets at subsonic speeds. Technical Report 86002, ESDU, April 1986.
- [21] F Pittaluga. A set of correlations proposed for diffuser performance prediction. *Mechanics Research Communications*, 8(3):161–168, 1981.
- [22] Petter Miltén, Isak Jonsson, Anders Lundbladh, and Carlos Xisto. Generalized method for the conceptual design of compact heat exchangers (unpublished).
- [23] C S Lin, N T Van Dresar, and M M Hasan. A pressure control analysis of cryogenic storage systems. Technical Memorandum NASA/TM-1991-194498, NASA, 1991.
- [24] Ian H. Bell, Jorrit Wronski, Sylvain Quoilin, and Vincent Lemort. Pure and pseudo-pure fluid thermophysical property evaluation and the open-source thermophysical property library coolprop. *Industrial & Engineering Chemistry Research*, 53(6):2498–2508, 2014. URL: http://pubs.acs.org/doi/abs/10.1021/ie4033999, arXiv:http://pubs.acs.org/doi/pdf/10.1021/ie4033999, doi:10.1021/ie4033999.
- [25] Frank P. Incropera, David P. Dewitt, Theodore L. Bergman, and Adrienne S. Lavine. *Incropera's Principles of Heat and Mass Transfer*. John Wiley Sons, 2017.
- [26] Dries Verstraete. *The Potential of Liquid Hydrogen for long range aircraft propulsion*. PhD thesis, Cranfield University, 2009.
- [27] C. W. Keller, G. R. Cunnington, and A. P. Glassford. Thermal performance of multilayer insulations. Contractor Report NASA/CR-1974-134477, NASA, 1974.
- [28] Charles H McLellan and Mark R Nicholas. An investigation of diffuser-resistance combinations in duct systems. Technical Report NACA-WR-L-329, NACA, 1942.
- [29] W.M. Kays and A.L. London. *Compact Heat Exchangers*. Krieger Publishing Company, 1998. URL: https://books.google.se/books?id=A08gAQAAMAAJ.
- [30] E Torenbeek. Synthesis of subsonic airplane design. 1982.